Available online at www.sciencedirect.com

Manufacturing Letters

Manufacturing Letters 41 (2024) 1080–1091

52nd SME North American Manufacturing Research Conference (NAMRC 52, 2024)

Pure copper extrusion Additive Manufacturing of lattice structures for enabling enhanced thermal efficiency in hydrogen production

Paolo Parenti*[a], Francesca Zaio[b],Matteo Ambrosetti [b], Stefano Foletti [a], Alessandra Beretta[b],Gianpiero Groppi [b], Enrico Tronconi [b], Bianca Maria Colosimo [a]

[a]*Politecnico di Milano, Dipartimento di Meccanica, via La Masa 1, 20156, Milan, Italy*
[b]*Politecnico di Milano, Dipartimento di Energia, via La Masa 34, 20156, Milan, Italy*

* Corresponding author. Tel.: +39 02 2399 8532; Fax: +39 02 2399 8532; E-mail address: paolo.parenti@polimi.it;

Abstract

The high geometrical complexity allowed by Additive Manufacturing (AM) of pure copper can support the development of more efficient catalytic supports that can enable the design of efficient reactors for key processes for energy transition, i.e., hydrogen production with methane steam reforming or CO_2 conversion to synthetic methane, thanks to the enhanced thermal conductivity of the catalytic support. Low relative density lattice geometries with open cell copper geometries can be adopted as catalyst supports in the new generation chemical reactors to improve the heat transfer. This work presents a manufacturability study about pure copper lattice filters produced via metal Extrusion AM i.e., via feedstock 3D printing and sintering. The results show that feasible parts design can be reached and produced and that heat-exchange performances can be increased with respect to conventional supports, as confirmed by lab-scale heat transfer tests. A specific metrological assessment based on CTscan data is implemented on the printed parts to qualify them and to ensure a good thermal coupling between the printed filters and the heat exchanger main tube elements.

Keywords: Copper AM; Bound Metal Deposition BMD; Lattice; CT Inspection; Heat Exchanger; Hydrogen;

1. Introduction

The capability of Metal 3D printing to improve products and process performances is a key enabler for the green transition which is moving toward more efficient production and use of energy sources. The ability to print intricate geometric structures in individual blocks, without assembly, is one of the keys to this success, especially when high-performance material is adopted. To unlock this enabling potential not only the 3D printing technology must guarantee these abilities, but it must also lead to sustainable production costs to foster its industrial adoption. The AM process selection, based on those drivers, is far from being an easy task since each process shows different behaviours in relation to the address application field of the printed components. Therefore, benefits are generated when a technology is proven to be applicable.

More efficient heat exchange coupled with a functional high geometrical complexity are two winning potentials of 3D printing that can be exploited to manufacture high-performance catalyst supports that can be employed in the new generation catalytic hydrogen production systems. These critical components improve the efficiency of chemical reactions by enabling the maximization of the exposed catalyst surface and at the same time heat transport between the core of the reactor and the heat source/sink. To achieve this goal, among the specific component designs adopted, the so-called POCS (Periodic Open Cellular Structures) was demonstrated to be one of the most performant especially when made by highly conductive materials such as Aluminium or Copper.

The 3D printing of these lightweight structures brings several manufacturing challenges since tight geometrical and dimensional accuracy requirements and the best material performance are asked.

This paper demonstrates that via a design-for-additive approach, fully functional pure copper POCS elements,

matching the thermal exchange requirements, can be designed for, and produced by the metal extrusion technology named Bound Metal Deposition (BMD).

1.1. State of the art

The geometric accuracy capability of additive processes, especially on internal geometries that can no longer be finished through post-built machining, is one of the drivers on which the various processes available are chosen.

When it comes to lattice structures with fine struts, accurate 3D printing of such components is not a given since to enable their full functionality these structures must present limited geometric deviations from design [1]. The achievable quality strongly depends on the 3D printing method used to manufacture the lattice structure and the control parameters of that method [2], [3]. The quality of the lattice structure is usually defined by surface roughness, dimensional accuracy, geometric accuracy, struts' imperfections, microstructural material inclusions, porosity, and residual stresses [4].

Therefore, not only the geometry matters but also printable materials since additive processes are not yet able to provide full coverage from this viewpoint. Pure copper is a key material from this point of view, given its extremely high thermal and electrical conductivity [5]. This material however turns out to be a difficult material to 3D print with traditional power-beam processes because of its high thermal conductivity and high reflectivity to light beams [6],[7]. Being able to print a material well means doing so while ensuring low porosity, good mechanical performance and low costs [8]. In this regard, polymer feedstock extrusion processes prove to be among the most economical solutions for printing metals with the advantage of being powderless, thus very portable, and easy to use [9]. These processes take advantage of polymer-metal feedstock blends and the well-established powder-technology route that involves sintering the parts in special ovens for densification [8]. In general, however, the low throughputs and limited accuracies of these processes often preclude their choice in industrial settings, giving way to more established processes such as L-PBF and EB-PBF, especially in heat exchangers and lattice-type structures where due to constraints on nozzle sizes of the extrusion processes [8]. There are very few examples where direct printing of lattice struts structures in metal using metal Fused Filament Fabrication (metal FFF), such as steel [10], titanium [11], alumina [12], or similar extrusion processes like the robocasting slurry methods [13], have been tried and in very rare cases a case study where components were tested. The main difficulties are not only related to the printability of such fine structures (especially when discontinuous paths are required to the nozzle layer by layer) with relatively large nozzle sizes but also to the sinterability of these structures [14].

From the materials point of view, however, there is one area, that of pure copper, where the inexpensive extrusion process does not disfigure in front of previous processes indeed where it can guarantee comparable material properties in many cases [15]. It has been shown that with metal FFF it is possible to print pure copper obtaining residual porosity of less than 3% with limited oxide content ensuring good thermal properties to sintered products. However, there are still limited application studies and almost no attempts to produce functional lattice structures with this process.

Regarding the lattice structures application for catalysis, one of the areas where these 3D printed lattice structures with high thermal conductivity can provide significant advantages is small-scale catalytic applications for energy-intensive processes [16], where the heat transfer provided by the catalytic support can unlock potential for the design of small-scale, energy-efficient reactors for a variety of processes, i.e., small scale hydrogen production with methane steam reforming [17], or synthetic methane production with CO_2 hydrogenation processes [18].

Conventional catalytic processes employ packed bed catalysts that are optimized to be operated in large-scale systems. Heat transfer in this kind of catalyst support mostly relies on convection: in large-scale systems, with reactors 5-10 meters long, gas flows at significantly high gas velocity and the turbulent motion guarantees sufficient heat supply or removal [19]. When scaling down the catalytic processes, to meet emerging trends i.e., of distributed hydrogen uses or design of reactors for CO_2 valorisation by hydrogenation, the conventional systems cannot be employed, since, in a small scale short reactor, operated at low flow velocity, packed bed are not able to provide adequate heat transfer for these processes. A solution to this problem is the application of thermally conductive catalytic supports (honeycombs, foams) made of different materials, as a function of the process requirements, can solve this issue by providing a static heat transfer mechanism that is not a function of the gas flow velocity [20]. The demonstration of the advantage provided by copper-based catalytic supports for these processes is critically discussed in [17]. Additive manufacturing of tailor-made structures can further improve the performances of these catalytic systems, as recently demonstrated for the Fisher-Tropsh application where, thanks to the addition of an external skin to the 3D printed scaffold, it was possible to improve the contact between structures and reactor tube and providing a 2-fold increment of the heat transfer and the process productivity [21]. Whereas for aluminium – which can be employed only in low-temperature processes, 3D printing is already commercially available, this is not the case for copper that needs to be employed in high-temperature processes.

In the past, the authors have previously attempted to produce both FOAM-type (i.e., random noncellular ordered) and lattice strut type copper lattice structures by an indirect method based on dip-spin coating to copper slurry paste of resinoid structures produced by 3D printing stereolithography method [22]. It has been shown that it is possible to obtain strut sizes in the order of 500 μm but, at the same time, that the method shows manufacturing errors. These differences concerning nominal geometries (such as strut bending, cross-sectional deformation, and solid buildup at nodes), might lead to discrepancies in the functional behaviour designed. They can induce different cell and strut diameters, than the geometrical model, leading to an actual variation in the relative density from nominal value.

In this type of geometries, one of the advantages of BMD over other powder processes is that it is powderless [8], minimising the risk of trapped powder (not properly cleaned during depowdering in powder-bed AM processes) being introduced into the reactor during use.

In this paper, we present a feasible production method for 3D printed pure copper catalytic substrates that is compatible with the adopted feedstock extrusion. The fabrication method based on the BMD process is introduced, after which the

morphological properties of the produced lattice-based substrate relevant for the catalytic application (cell size, relative density, total porosity, surface-to-volume ratio) are presented. Finally, the heat transfer properties are experimentally characterized using tests carried out up to 550°C to understand the overall heat transfer in process-relevant conditions.

2. Design specifications for the pure copper catalytic support

The most important design input for the geometry of the POCS substrate for catalytic applications is the relative density of the lattice structure, i.e., the ratio of the volume occupied by the copper to the total volume of the component. On the one hand, it must be very small to allow the loading of a high quantity of catalyst agents, while reducing the pressure losses of circulating gases, and this is achieved with small pores and cells, resulting in small lattice strut diameters.

On the other hand, the structural stability of the lattice structure and the effective heat transfer are connected to the solid content.

This value is the main variable for evaluating the printability of the lattice structures considering the limits of the material extrusion process.

Another key aspect for catalytic structures activated by depositing a thin layer of catalyst onto the metallic surface is the surface area, which, at fixed solid content and cell shape, is inversely proportional to the strut thickness. In general, high surface area structures are desired to maximize the exposed surface and the catalyst loading while keeping the catalyst thickness under critical values that hinder noble-metal utilization.

The mechanical strength of the structure and the material is also critical since they must withstand the thermo-mechanical stresses happening both during the lattice support assembly/mounting in the main plant tubes, during the loading of catalysing agents and during the hot exposure when in functioning. For this reason, it is a good idea for the printed material to have the most sintered density i.e., with little residual internal porosity (which also impairs thermal transfer).

To minimise as much as possible the contact thermal resistance between the lattice and the outer walls of the tube inside which they are inserted into the reactor, it is best to print with an outer skin, with the minimum thickness possible, to minimise thermal contact resistance.

If the lattice structure is printed inside this material liner (the external shield/skin) to ensure good thermal coupling of the struts with the reactor tubes, it is also a good idea to ensure the gas-tightness of this liner to avoid unnecessary additional pressure losses due to leakage. From the point of view of dimensional and geometric specifications, it is a good idea for the struts and cells to be homogeneous and regular to avoid thermal and catalyst loading imbalances. The external liner geometry instead is critical since its shape must guarantee a fitting in the external tube with the design coupling load.

While the external roughness of the liner should be minimized to guarantee the coupling contact with the receiving tube, there are no clear requirements regarding the roughness of the internal strut structure. The operation in the reactor is governed by conduction heat transfer, so the increased exchange surface area associated with increased strut roughness could even be positive (provided the relative design density is guaranteed) and favours the catalyst adhesion. On the opposite, a less relevant effect of the lattice roughness on the fluid-dynamic and pressure drop actions is expected.

3. Design-for-metal extrusion AM

Based on the information available in the current scientific literature, and on the knowledge shared by the technology providers, it is not possible to assess a priori the printability of a lightweight lattice structure by a metal feedstock extrusion system, utilising pure copper material.

In this challenge, many variables come into play both on the printability of the structure and its sinterability in the oven when using a type of metal AM process chain.

For its intrinsic characteristics of having a printed filament continuously flowing out from a nozzle, the Fused Deposition Modelling printing method, used by metal extrusion systems, can efficiently print surface-type lattices (as TPMS geometries [14]) but might struggle with strut-type lattices due to the necessity to extremely discontinuous deposition on each layer. Strut Lattice printing is resource-intensive due to its intricate architecture and multiple nodal connections which require the extruder to jump from one strut to another for very little material deposition.

The main constraint on printability is the minimum feature size that the machine and nozzle used allow. The thinnest wall or the smallest geometric feature cannot be smaller than approximately twice the diameter of the nozzle used, that typically ranges from ϕ_{nozzle}=0.25 to 0.4 mm. Even considering the shrinking in the furnace (up to 17-18% for most of the metals) which reduces the final part size, this is a strong limitation.

In the case of lattice structures, there is an additional constraint to consider, namely the overhang constraint which regards the maximum length of the inclined cantilevered section without supports that the machine is capable of printing and sintering with good quality). This threshold is linked to the strength and density of the green material used and its ability to bond layer by layer as a function of the temperature at which it is laid (e.g., 150-200°). The density of the metal feedstock is 4-5 times greater than the pure thermoplastic polymer density, therefore the overhang limits typically differ than standard polymer FDM and need specific evaluation for each metal feedstock material.

The printing of self-supporting lattice structures is often required due to the impossibility of removing the printed supports inside tiny structures, which limits the achievable minimum lattice cell size. The use of the ceramic interlayer for the supports, available in some extrusion technologies such as the BMD used in this study, could be used to design breakable supports that can exit from tiny gaps but the tendency of the ceramic interlayer to increase sintering stresses and to contaminate the interfacial zones with some embedded alumina particles in the copper (evidently incompatible with the operation of the structure in the catalytic reactor due to the possible release of contaminants) drives toward a support-less design. In metal extrusion, it is prescribable to print a raft base upon which the component structure can shrink in the sintering oven with reduced friction while reducing the sintering stresses. The thickness control of this part is critical, especially in the presence of large footprints, for the above-mentioned thermal issues. This part help also controls the warping tendency of the printed structures. It must be paid attention that

wall thickness in all the parts, should not exceed about 10 mm full (dense) wall to respect the debindability limits (that guarantee a proper binder dissolution in the solvent cleaning phase. At the same time, given the target thermal conduction functionality, the use of infill within those walls is not suggested.

While printing the green component, the tendency of the extrusion nozzle to deposit stringing is also a potentially limiting problem for the quality of the lattice printings, which must be carefully avoided by managing material feed/retraction control policies, print temperatures and nozzle rapid trajectories.

Once the printing phase is completed the sinterability of the components must be assessed since it is not certain that a tiny supportless printed lattice structure survives the sintering intact. The inherent weight of unsupported structures could lead to their collapse at the stage when the backbone component of the binder is removed at the end of thermal debinding in the furnace. Moreover, in sintering, the taller the part, the bigger the self-load stresses on the structure and in the case of struts bigger than nozzle diameters, it is advisable to introduce connection radii between them to avoid stress intensification. Design is fundamental since a poor part design could easily bring to encounter a partial or even total structure collapse in the oven.

From the point of view of the final sintered part density, as in the standard geometries, it can be maximized by printing the densest green parts possible (by avoiding air gaps) and by tuning the thermal sintering cycle properly (heating rates, holdings, and max temperature) to allow the best possible densification (minimizing microporosity).

4. Experimental method

Rhinoceros and Grasshopper software equipped with the IntraLattice and Dendro plug-ins were used to design the lattice component. Materialise Magics software is used for mesh healing and coarsening.

The Desktop Metal Studio System + [23] consisting of three units namely the printer, debinder and Argon+3%Hydrogen sintering furnace is adopted, Figure 1. The pure copper material is supplied by the machine manufacturer in the form of rods with a diameter of 6 mm and a length of 150 mm. The binder composition adopted for the feedstock is not disclosed but it generally consists of a multi-component thermoplastic-based material (wax + backbone + additives). Debinding first takes place in solvent through a warm 1.2-dichloroethylene bath. Sintering involves the use of graphite setters and ceramic bases on which the parts are placed. The sintering cycle adopted is the prescribed one by the machine supplier, which reaches 1060°. Zirconium oxide getters are used in sintering to keep the atmosphere as free of contaminants as possible, ensuring the purest possible sintered copper. At the end of sintering, the part is measured with a micro-CT scan of the General Electric type of Phoenix V|TOME|X M 180KV/300KV with a voxel size of the reconstructed three-dimensional model (i.e., the size of the volumetric pixel) of 15 μm. The Sartorius method is adopted for porosity estimation. Surface roughness measurements are conducted on an Alicona G6 Focus variation microscope. The heat transfer setup for the thermal conductivity measurements is described in section 5.1.

4.1. CTscan Analysis Methods

Measurements are conducted with the VGstudio software and with specially developed MATLAB routines that analyse the high-density point clouds and the lattice components [24]. The morphology of the printed lattice struts is studied with Strut Surf software [25] by feeding it with 5 * 5 * 5 mm regions of interest extracted from the main lattice structure at half of the sample radius at four different height levels from the base (5,10,15,20 mm).

4.2. Tested design of the printed catalyst support

The design of the 3D printed substrate provides a lattice structure with a relative density of 15 per cent and a diamond cell type with a nominal strut size of 0.6 mm with a cell size of 3 mm. These dimensions are a design feature to ensure the maximum and smoothest possible fillability with the catalyst agent spheres while still allowing a match with the BMD process capabilities. Three longitudinal holes (with a diameter of 2.1 mm and thickness of 1 mm, in the centre and 11 and 14 mm from it, respectively) are provided to allow the housing of thermocouples that measure the radial and longitudinal temperature profile during heat transfer tests.

The part has a 1.5 mm thick outer cylindrical shell with flat faces at the two ends (to allow for specimen stacking) and has dimensions of ϕ=33.9 mm and H=36.25 mm.

4.3. Printing process setup and parameters

The created STL model required the control of the mesh size to be loaded into the printer's slicer, since this shows a limit on file size of 128 Mbyte. The mesh coarsening level was optimised precisely to fit within this limit. The mesh coarsening introduces geometric roughness on the struts but in the case of the catalytic filter, these are filtered out by the printing process. However, slight nominal struts' size errors are also introduced by the coarsening as discussed in the results section.

Vertical orientation is selected for both the printing and the sintering of the lattice filter allowing a support-less processing. The selected nozzle size was 250 μm. The optimal setup conditions, in terms of printing parameters, were found as temperatures set to 170°C and 60 °C for the extrusion nozzle and the bed, respectively. Line Width and Layer Height are set to 0.3 and 0.1 mm, respectively. The deposition speed used is 12.5 mm/s.

The sliced path used is the proprietary Ultrafine+ printing strategy. The adopted base i.e., the raft, is selected as the convex hull of the component, with a height of 2 mm (20 layers) separated by 3 layers of a conformal ceramic interface. A random Z seam alignment is used layer-by-layer.

Nozzle purging operations are prescribed for every loading of the new material rod into the extruder (five copper rods are needed to print the whole geometry). The guidelines provided by the manufacturer in terms of shrinkage factors are confirmed to be optimal and therefore the nominal oversize factors for compensating the sintering shrinkage factors are adopted as 18%, 18%, and 19% respectively in X, Y, Z.

To avoid infill generation in the cylindrical liner, a wall thickness equal to 1 mm is selected. The green part mass is 123.51 g, the brown part 119.19 g, and a final part mass is 88.82 g. A total number of 455 layers are printed. Printing Time of each filter is 37.9 hours, Debinding time is 9 hours, and the total Sintering time is 42 hours.

4.4. Sample Loading into the main copper liner

After the sintered part is obtained, a special loading procedure was designed to maximize the heat transfer performances of the sample, avoiding the machining of the lattice support. It is in fact very complex to control in detail the external part diameter since the sample, as typical for many sintered products, is prone to display a smaller diameter at the top and a higher diameter at the bottom of the sample, i.e., elephant foot defect. It was decided not to load the sample directly in the tube used for heat transfer tests but to use an additional copper liner to reduce the impact of the possible printing defects. The heating tube is a stainless steel reactor with external flanges, the dimensions in the testing regions are ID = 36.00 mm +/- 0.01 mm and the OD is equal to 42 mm, giving to the structure good mechanical stability. A copper liner was derived from commercial copper tubes by lathe turning with an external diameter of 36.02 mm +/ 0.01 mm. and an internal diameter of 33.85 +/- 0.01 mm. The 3D printed sample was first cooled in liquid nitrogen and then loaded in the copper liner thanks to a manual press (SPECAC, 5 tonnes loading), by using a stainless steel pastil placed on the surface of the POCS to avoid the direct application of the force on the struts and avoid structure deformation. This loading process helps maximize the thermal contact between the structure and the liner surface thanks to the combination of the cooling action and the controlled loading procedure. A similar procedure was then applied to load the liner and the structure into the stainless steel tube, cooling again the copper structures in liquid nitrogen. In this case, the selected difference between the liner diameter and the tube diameter was smaller, given the perceived lower elasticity of the copper liner concerning the copper lattice structural portion.

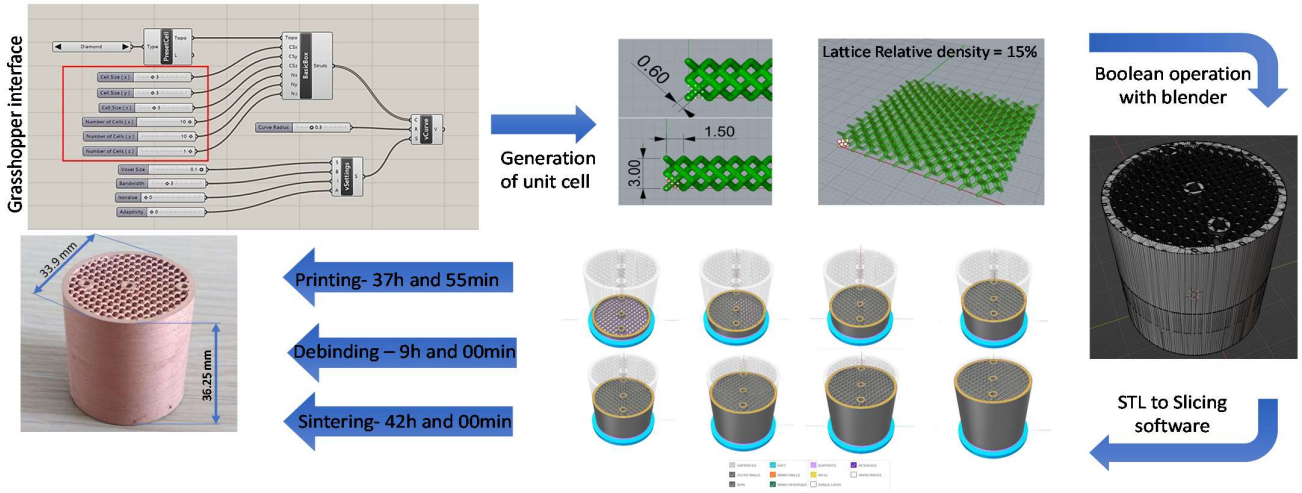

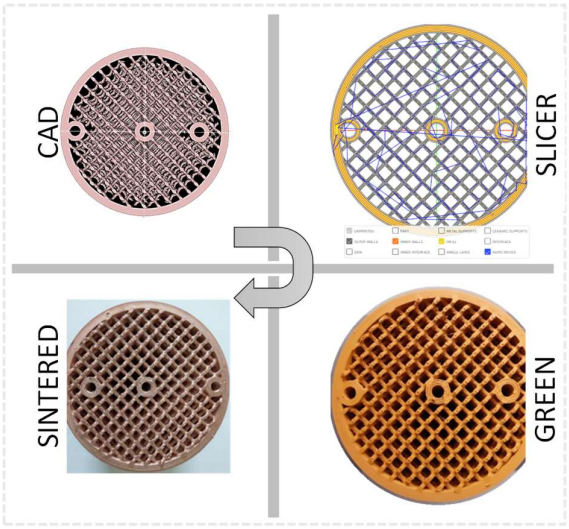

Figure 1: Design and manufacturing route of the pure copper catalyst lattice support (conceptual flowchart and designed vs. printed parts)

5. Heat transfer

5.1. Heat transfer setup and test procedures

The heat transfer performance of copper POCS was evaluated by running non-reactive heat transfer experiments under steady-state conditions. Tests were performed by flowing an inert mixture, composed of nitrogen with 1% of hydrogen flow to prevent copper oxidation at high temperatures (given possible oxygen traces in the N_2 stream that could have a dramatic effect on the structure stability); total flow rates fed to the system are equal to 10 l/min and 30 l/min, both streams are regulated by mass flow controllers (Brooks 5810). The stainless-steel heating tube was then connected to the gas-feeding system and loaded into a thermostatic chamber that was set at a constant heating temperature (Mazzali thermotester). Eight aluminium fins in the shape of two separated blocks are placed around the reactor tube to improve heat transfer, screwed tightly on the reactor tube to avoid any contact resistance. To allow uniform flow distribution at the reactor inlet, Al_2O_3 pellets with a 3.5 mm nominal diameter were placed at the reactor inlet (Figure 2). Copper structures were tested starting from an oven temperature of 200°C, which was then increased up to 550°C; to check the reproducibility of the results, at the end of the experimental campaign, a heat transfer test at an oven temperature equal to 200°C was

replicated. Axial temperature profiles were collected at 4 different radial positions, which are indicated with red dots in (Figure 2): centerline (C), at a radius equal to 11 mm and 14 mm (R11 and R14, respectively) and external reactor wall (W). The 4 K-type thermocouples were linked to a Zaber linear stage to collect temperature samples at every 1 mm along the reactor length.

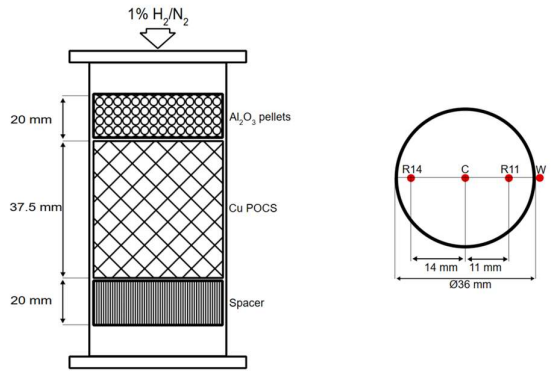

Figure 2: Reactor scheme for heat transfer tests with four temperature probs (red dots). Cu POCS indicates the produced 3d printed part

5.2. Estimation of overall heat transfer coefficients

The overall heat transfer performance (at different flow rates and temperatures) was quantified by a 1D model analysis, assuming that the thermocouples are measuring the gas temperature. The steady-state 1D energy balance in temperature form can be written as:

$$\rho_{gas}\, u\, c_P\, \frac{dT_{cupmix}}{dz} = \frac{4\, U_{overall}}{d_{tube}} \left(T_{wall} - T_{cupmix}\right) \quad (1)$$

where T_{cupmix} is the mean-cup temperature of the fluid that represents the radially averaged temperature for a given axial position, ρ_{gas} is gas density [kg/m^3], u is the fluid velocity [m/s], c_p is the specific heat [J/kg/K] and d_{tube} is the heating tube diameter (equal to 0.036 m). We neglect possible heat transfer resistance provided by the tube thickness, given the high conductivity of pure stainless steel. Assuming negligible dependency of constant gas heat capacity on temperature and an ideal plug flow behavior, the cupmix temperature for each axial point can be calculated as follows:

$$T_{cupmix} = \frac{\int_0^{R_{tube}} 2\pi\, T(r)\, r\, dr}{\int_0^{R_{tube}} 2\pi\, r\, dr} \quad (2)$$

Radial temperature profiles (T(r)) for each axial position (z) were evaluated by interpolating the three axial temperature profiles collected from experiments (r = 0 mm, r = 11 mm and r = 14 mm) with the 4th-order symmetric polynomial,

$$T(r) = T(r=0) + A\, r^2 + B\, r^4 \quad (3)$$

where A and B can be determined analytically.

Assuming constant fluid properties, the analytical solution is given by:

$$T_{cupmix}(z) = T_{wall} - \left(T_{wall} - T_{cupmix,z=0}\right) \exp\left(-\frac{4\, U_{overall}\, z}{\rho_{gas}\, u\, c_P\, d_{tube}}\right), \quad (4)$$

where T_{wall} is the axially average wall temperature, $T_{cupmiz,z=0}$ is the minimum temperature of the system, and $T_{cupmix}(z)$ is the cup mix temperature in the actual axial position z. By linearization of the proposed equation, it is possible to estimate $U_{overall}$ by linear regression analysis of the experimental data.

6. 3D printing results

The components were successfully printed and survived the sintering cycles, resulting free from visible cracking. The sintering operation in a reducing atmosphere resulted in an acceptable densification and good grain formation, as confirmed by the SEM analysis carried out on sample material, (Figure 3).

Bulk material presents a minor fraction of the sintering microporosity localized at grain boundaries.

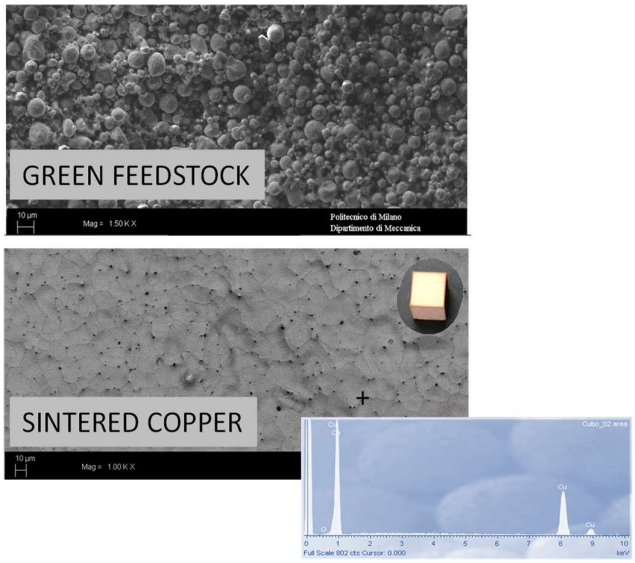

Figure 3: SEM analysis on the green-state feedstock and sintered-state material

6.1. STL error on the relative density

The STL discretization adopted for the component gave an average diameter of 0.562+-6 µm (smaller than the design datum of 0.6 mm). The relative density of the printed STL moves from the designed 15% to 16% even though the struts have a smaller average diameter. These deviations are attributable to the modelling software and the level of mesh coarsening used and are only partly easily compensated for.

6.1.1. *Overall part dimensions*

Regarding the dimensions of the sintered parts, the geometry deviation value indicates that 90% of the surface of the object is in the range of up to 0.3 mm (100% of the geometry deviations are in the range of up to 0.5 mm), Figure 4 and Table 1.

The sintered cylinders containing the lattice are slightly oval and bulging, i.e., with a larger external diameter at the base and smaller at the top. The causes are to be found in the uneven volumetric shrinkage caused by the furnace sintering and the load effects of the self-load. To a lesser extent, the uneven

friction effects of the component with the ceramic base during the shrinkage motion could also have contributed to these errors. The average errors on the main diameters of the component are -0.21 mm (0.62%), 0.02 mm (0.059%) at the base and -0.64 mm (1.88%), -0.37 mm (1.1%) at the high end, in X and Y direction respectively.

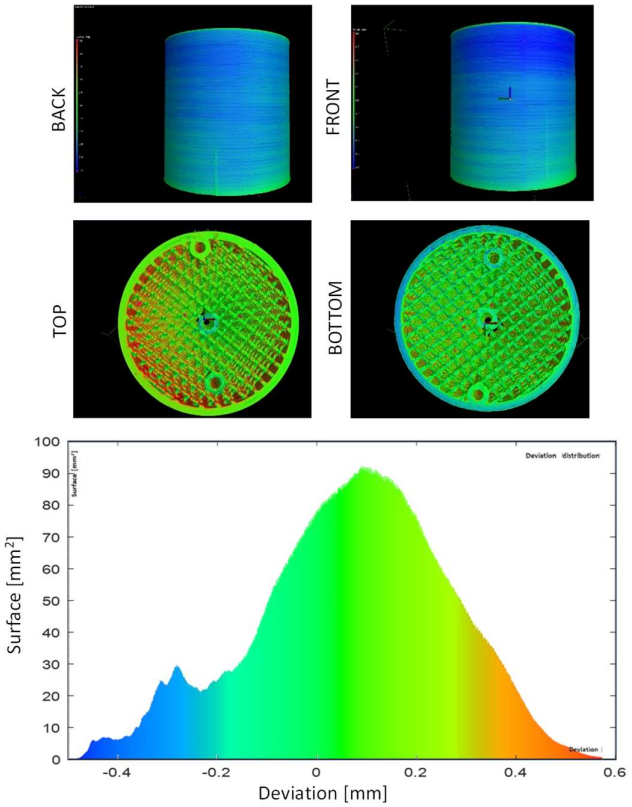

Figure 4: Nominal vs. Actual geometrical comparison analysis on the part (performed using VGstudio software)

Table 1: Dimensional Errors on the sintered part

Nominal Part	Actual Part				
	Bottom (mm)		Top (mm)		Height (mm)
X*Y*Z	X	Y	X	Y	Z
33.9*33.9*36.25	33.69	33.92	33.26	33.53	36.54
Deviation (mm)	-0.21	0.02	-0.64	-0.37	0.29

The total height of the test specimens is on average 0.29 mm (0.8 %) higher than the nominal value (36.25 mm).

The wall thickness of the cylindrical shell is irregular and shows differences with both the axial and angular coordinates (Figure 5). On average, its value is 1.474 mm or 26 µm smaller than expected (error of -1.8%). The fact that the part appears oval-shaped seems to be caused in part by the variation in tube thickness with the angular coordinate, especially at higher coordinates (levels 4 and 5).

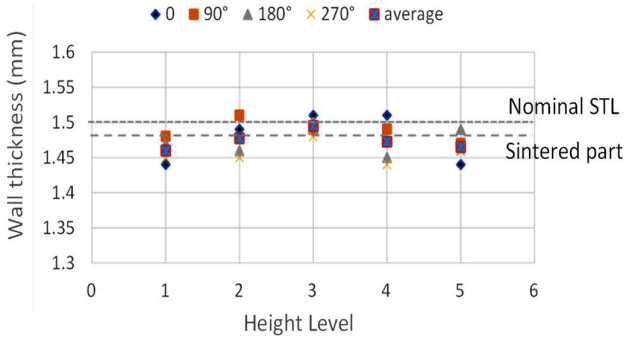

Figure 5: External wall thickness values (measured on the cylindrical shell of the parts) as a function of the radial and the axial part coordinates (height level)

6.1.2. Porosity

From the point of view of porosity, the cylindrical shell shows the presence of elongated (low sphericity) pores, located between strand and strand but also between layer and layer, Figure 6. These pores are compatible with the chosen deposition path (concentric) and the under-extrusion phenomenon. The detected air-gaps porosity by the CTscan is then quantified as 1.05% with a maximum and minimum diameter of pore size of 7.795 mm and 0.071 mm, respectively, Figure 6. The same is true for the walls of the internal thermocouple access holes but in an even more pronounced manner.

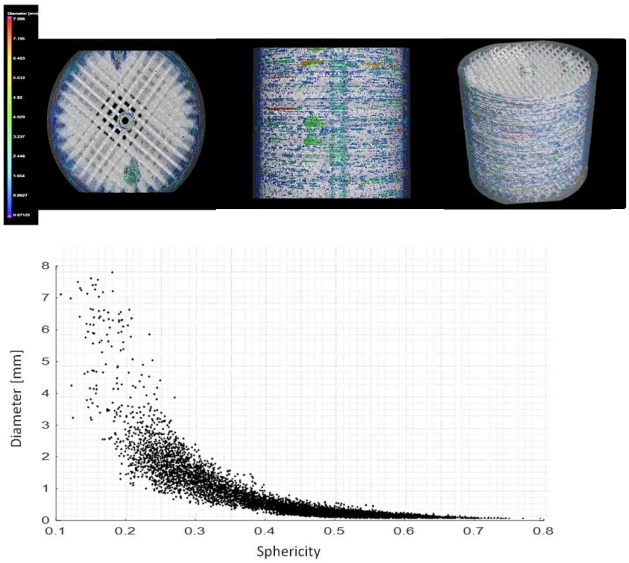

Figure 6: Internal Porosity analysis results: spatial distribution of the pores and pore sphericity analysis ((performed using VGstudio software)

This fact indicates a potential limitation for the heat exchange and therefore requires attention in terms of optimization of the printing strategies. No air gap pores are found internally in the lattice struts regions. It is expected that lattice regions contain microporosity as the other bulkier part regions (the resolution of the CTscan cannot capture them). To confirm that, Sartorius tests are executed on the filters giving an overall average porosity of 3.3% on the parts. It is noted that the connecting region between one of the thermocouple access holes and the tube is subjected to localized air gap formation which requires the adoption of different process toolpaths to be minimized.

6.1.3. Roughness of the tube

In terms of roughness, the external surface of the as-built tube shows an average aerial surface roughness equal to Sa= 19±4 µm (cut-off 800 µm) but shows blob defects with an average radius of 0.08 mm randomly localized among the layer and along the radial coordinates (Figure 7).

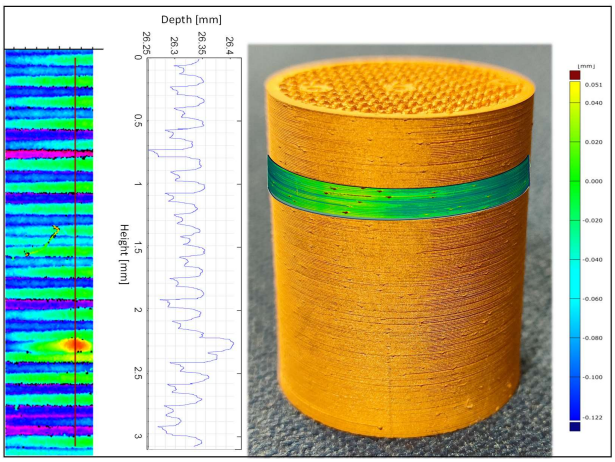

Figure 7: Surface roughness on the external shell surface (measured via Focus variation Alicona G6 microscope)

These defects are caused by the release of material build-up around the nozzle. It is observed that this adhered material accumulates during the deposition of the struts and is cleaned during the tube perimeter deposition. Due to their small extensions, these defects do not represent a problem for the assembly of the tube, even if a possible small impact on the local contact resistance cannot be excluded.

6.1.4. *Characterization of lattice struts and relative density*

From the point of view of lattice structure, the struts were mostly coming out from sintering as intact. However, they have obvious defects and show high irregularity and variability. Most of them are already present in the green state parts as they are caused by the printing process (Table 2). Blobs, staircase effects, oozing, and protrusions, under extrusion, were observed on the surface of the lattice struts (Figure 8). It has been observed that during the point-to-point deposition required by the lattice diamond cell adopted, the nozzle accumulates material build-up whose eventual random release during the deposition causes the blobs and protrusions on the lattices. The presence of the external tube appeared to be beneficial in this sense since it requires a continuous trajectory where the nozzle can clean itself.

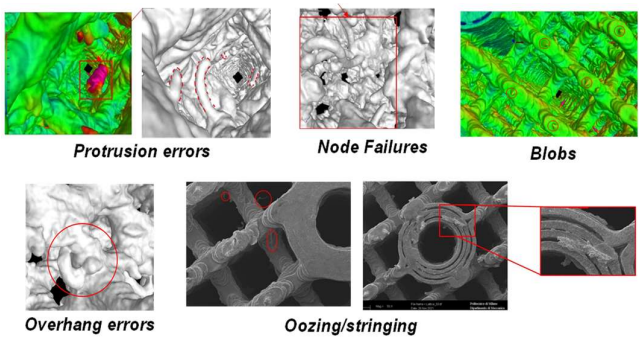

Figure 8: Defect mapping on the 3d printed struts

These defects cause variation of the internal geometry of the sintered part which shows an average relative density that is 2.93 percentage points higher than the STL file (i.e., RD = 18.93%), which in comparison to the design datum of 15% shows a deviation of 3.93 percentage points, Figure 9. The relative density value tends to vary along the axial coordinate of the part by a random amount of +- 0.25 %. The top level of the part shows the biggest deviations.

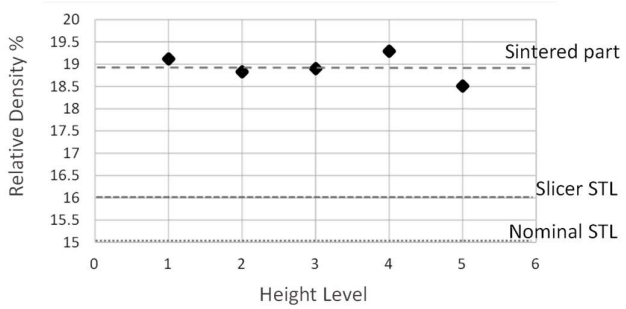

Figure 9: Measured relative density (of the lattice structure contained in the parts), as a function of the part axial coordinate (i.e., height level)

Table 2: Classification of defects found on the lattice struts

Defect type on struts	Description	Location	Occurrence	Effect on functionality
Strut cross section mismatch	excess of deposited material (struts have larger cross section area)	Radial and axial (bigger at the base and external perimeter)	Printing /Sintering	Bigger RD%, reduced and anisotropic catalyst loading, Bigger Mechanical resistance (Axially /Radially)
Strut cross section eccentricity	Struts section area is mostly elliptical. Average eccentricity e=0.49	radial and axial (Random)	Printing	Possible anisotropy of Mechanical resistance in radial and axial direction. Effect on assembly, catalyst loading, and thermal fatigue
Struts blobs	over-deposition marks where nozzle leaves the struts	Only upper face struts	Printing	none
Protrusions	Left over material (stringing and filaments) trapped in the lattice among the struts	Random	Printing	Reduced and Anisotropic catalyst loading in the affected cell
Contamination with Alumina	Struts in contact with ceramic interlayer for support removal show particle contaminants of alumina	Bottom face of the struts in contact with the raft	Sintering	Contamination of the reactor (require surface cleaning before use)

In the diamond lattice unit cell, the struts can be classified into two groups formed by the V-Type struts (the struts lying above the nodal point), and the inverted V-Type, i.e., the struts lying below the nodal point. From these preliminary investigations about the geometrical errors, it seems that there are some systematic differences between these two groups in terms of areal accuracy and roughness. This confirms the strong coupling between the geometrical part complexity and the extrusion path in the quality determination of the printed lattice. Inverted V-type strut pairs seem to be more homogeneous in terms of cross-section area and surface roughness. This latter seems to gently increase with the level of height from the bottom (Figure 10). The tendency to present different lattice quality with the height is not new in AM processes but here is particularly pronounced. The cross-section area of all the struts gets closer to the nominal value (0.28 mm^2) only at the minimum height level (Height Level 1 in the boxplot in Figure 10). Larger areas and larger dispersion are noticeable at the height levels 2 and 3.

Interestingly, by looking more in detail to V and inverted V-Type struts, the cross-sectional area of struts d and h increases with the level of height whereas c and g decrease with the level of height. This complex, but systematic, "axial" dependency could have been generated by the accumulation of material build-up around the nozzle (somehow proportional to deposited length), but it could also have interacted with the layer temperature evolution that presumably shows some dependency with the height level.

Regarding the presence of protrusions, caused by excess material accumulation at the nodes and improper cooling effects of the material, the two types of struts show different behaviours, and this is interesting since catalyst particles in lattice architectures for filter applications may be hindered by obstructions inside predefined pores. In general, protrusions across the node/struts at the top level are more than at the bottom. The protrusions can be seen more at the place of node X (junction of V-type and inverted V-type struts joins at same plane) and tend to flow towards the direction of adjacent V-type struts. Node X shows a better response in terms of geometrical deviation, but Node Y has generally a good surface and fewer defects. From the observation, either one of the struts from the same node exhibits a higher area, and the other one is smaller. Likewise, one strut has a large area that also it receives material from the node. The width of the struts also increases by excess accumulation at the node. Because of this lesser strut on the other side, an increase in inclined angle occurs. This increased inclined angle tends to increase the surface roughness. This occurs due to excess overhang. These phenomena of improper fusion in the lattice show some tendency concerning the height from the start of the building.

The variations in the cross-sectional area of the struts and the presence of local defects as a function of the vertical coordinate of the part surely contribute to the systematic geometrical error of the part concerning nominal shape.

By looking at the overall areal deviation layer-by-layer (Figure 11) one can notice that the deviation trend of the overall layer area along the height coordinate becomes extremely clear and quantified in a relative variation of the error from bottom to top of about +40%.

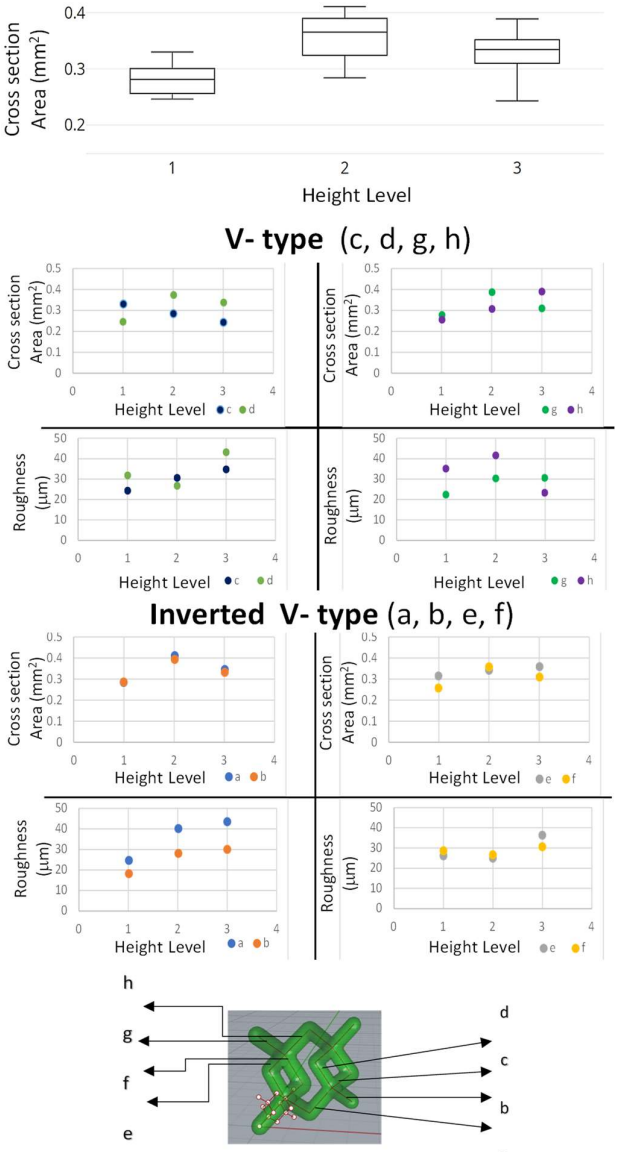

Figure 10: Cross-section area and roughness of the struts composing the lattice structure (measured on the CTscan point clouds)

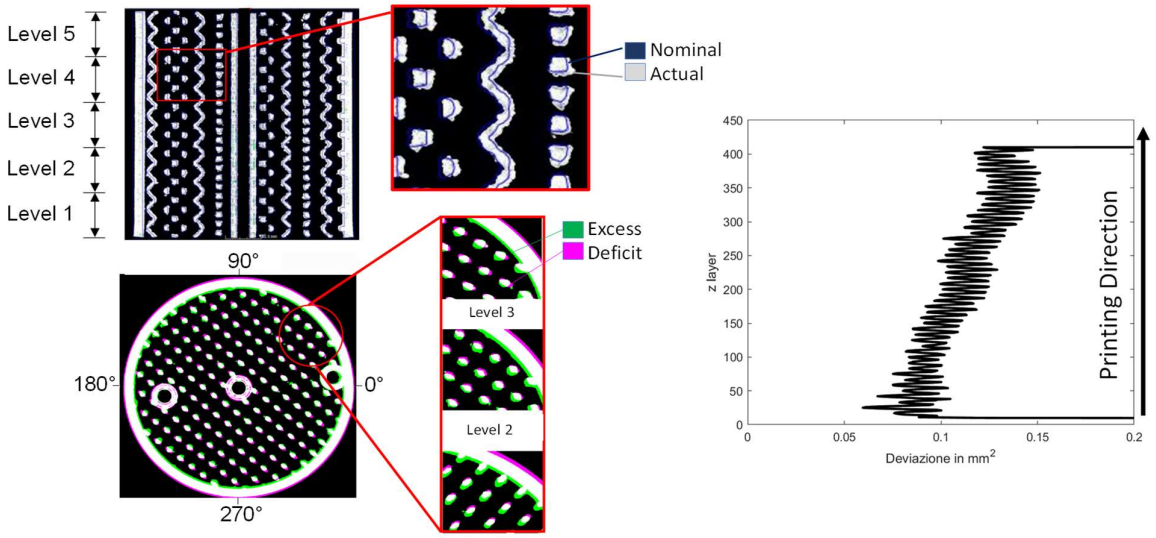

Figure 11: Spatial mapping of the printing errors on the printed part (the actual geometry over imposed on the nominal one) (a). Layer-by-layer areal deviation of the lattice section area (actual measured value vs. nominal one).

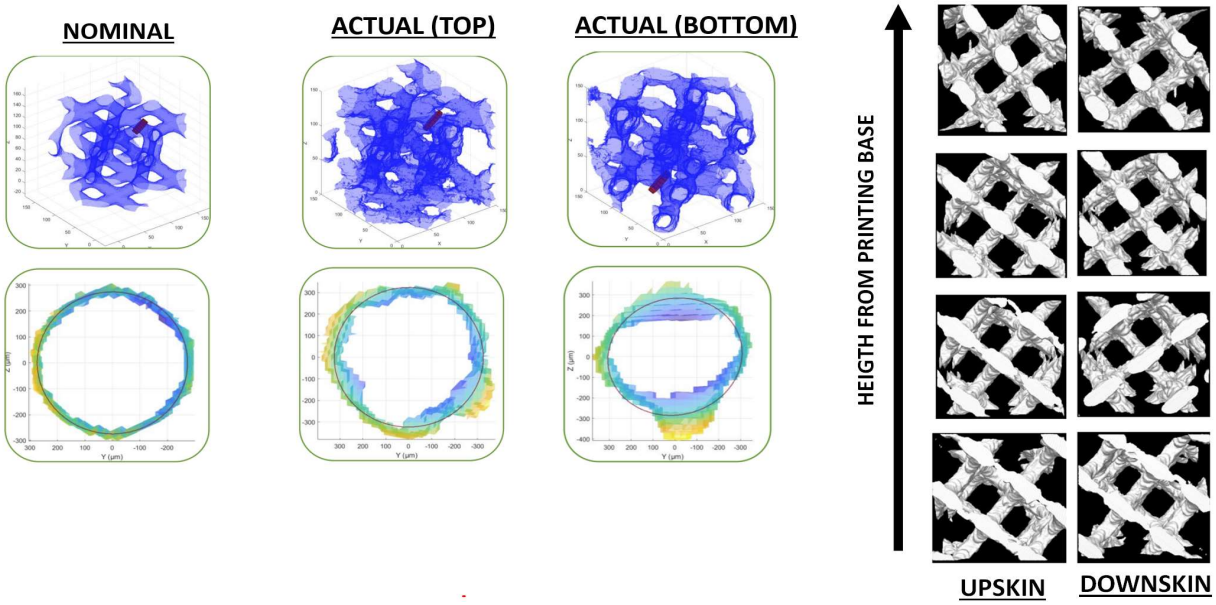

Figure 12: Shape analysis on the lattice struts: geometrical fitting on the cross-section area and CTcan image inspections

Finally, it can be observed that these defects in the shape generation of the struts cause not only an area dimensional variation but also a deviation in the morphology of the struts that tend to become more elliptical (Figure 12) at higher Z coordinates.

In any case, it is confirmed by inspecting the upskin and downskin surfaces that downskin features have much coarser definitions in comparison to upskin from all levels of height coordinate (Figure 12). This was expected, similarly to other metal AM processes, as originated by the support-less processing adopted.

6.2. Heat transfer experiments and evaluation of heat transfer coefficients

Figure 13 shows axial temperature profiles collected at T_{oven} = 200°C, with a flow rate equal to 10 l/min (Figure 13a) and 30 l/min (Figure 13b) and at T_{oven} = 550°C, with a flow rate equal to 10 l/min and 30 l/min (Figure 13c and 13d, respectively). As described before, temperature sampling along the axial coordinate was performed at the centerline, at r = 11 mm, at r = 14 mm and the external reactor wall (indicated with black, grey, blue and orange diamonds, respectively). Looking at Figure 13a, at the reactor inlet (which is located at a reactor length equal to 2 cm) the axial temperature gradient in the POCS structure is higher, then temperatures increase along the axial coordinate and approach the external wall temperature at the reactor outlet (reactor length equal to 5.8 cm) This can be explained by expecting that the first portion of the temperature profile is controlled by gas/solid and in the second part, once thermal equilibrium is reached the temperature profile is mostly controlled by the effective thermal conductivity and the wall heat transfer coefficient.

The system is characterized by low radial temperature gradients, as expected from previous findings [26]. The same behavior can be observed by running the test with a higher flow rate (Figure 13b); however, lower internal POCS temperatures can be observed. Moreover, the system is not able to approach the temperature measured at the external reactor wall. The higher the flow rate, the higher the flowing heat capacity that is entering the system, which implies lower axial temperature profiles.

The same features can be observed for the experiments performed at T_{oven} 550°C, with flow rate equal to 10 l/min and 30 l/min (Figures 13c and 13d).

The estimates of POCS heat transfer coefficients ($U_{overall}$) are plotted against the oven temperatures investigated and presented in Figure (orange diamonds).

Overall heat transfer coefficients increase with increasing flow rate for all the investigated oven temperatures; this behavior can be explained by a residual gas/solid heat transfer limitation that progressively is reduced.

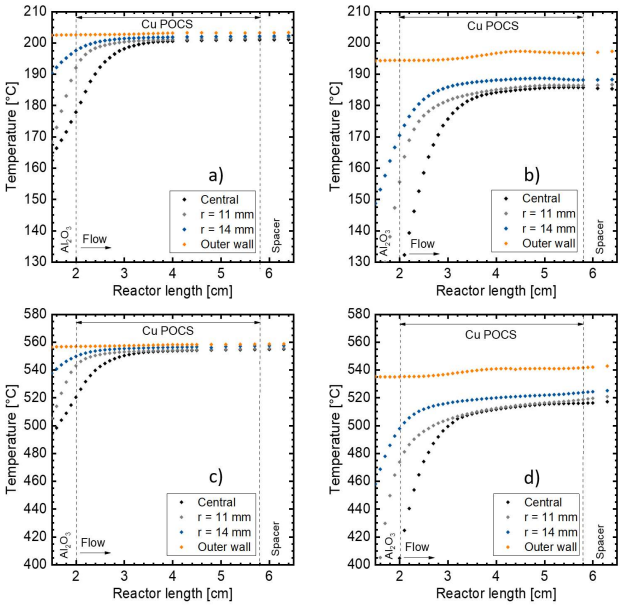

Figure 13: Results of thermal testing on the parts: Axial temperature profiles for T_{oven} = 200°C, Q= 10 l/min (a) and Q = 30 l/min (b) and T_{oven} = 550°C, Q = 10 l/min (c), Q = 30 l/min (d)

Overall, the replicated test performed at T_{oven} = 200°C is reported in the figure (labelled as "Repetition"); results are well aligned with the previous test, with axial temperature profiles like the one presented in Figure 14, showing that the thermal contact provided by the loading method is not worsening by operating the system up to 550 °C.

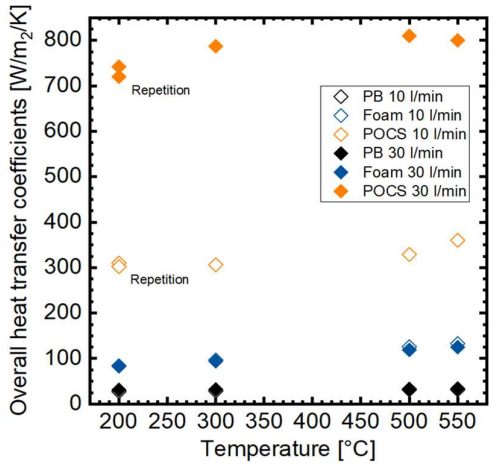

Figure 14: Results of thermal testing on the parts: Overall heat transfer coefficients for Packed Bed, open-cell foams and POCS at Q = 10 l/min (empty diamonds coloured borders) and Q = 30 l/min (solidly coloured diamonds)

POCS overall heat transfer coefficients are then compared to the one computed for the Packed Bed configuration (indicated in Figure 14 as "PB", black diamonds, which represents the traditional steam reforming configuration) considering a pellet nominal diameter equal to the one of the POCS structure (d_{pellet} = 3 mm, ε = 0.38, λ_{pellet} = 1 W/m/K) and open-cell foams copper foam with the same copper relative density of the lattice employed in this work with same POCS cell diameter (λ_{copper} = 400 W/m/K, d_{cell} = 3 mm) indicated in Figure 14 as "Foam", blue diamonds) POCS structure clearly leads to the enhancement of heat transfer properties concerning Packed Bed thanks to the thermal conductivity of copper and the interconnected structure. The advantages over the foam structures can instead be explained by the higher gas/solid heat transfer rates provided by the diamond cell geometry and thanks to the presence of the external skin that maximizes the contact between the structure and the reactor walls.

7. Conclusions

This work has shown that the Bound Metal Deposition, a metal extrusion process can be used to manufacture functional pure copper lattice supports (ϕ=0.6mm), which can be used as critical components for the enhanced heat exchange inside a catalytic reactor. Replicated heat transfer tests at 550°C confirm the structural integrity of the component even after several cycles of thermal stress, suggesting sufficient structural integrity of the printed components. The key steps for achieving this success are the application of design-for-metal extrusion AM rules along with an optimal 3D printing process design. This consists of specific selection of process parameters, including the non-standard use of a 0.25 mm nozzle, the use of support-free printing and the management of the geometrical distortions and dimensional deviations on the printed components. The most important aspect to consider is the tendency of the printer to over-deposition, which systematically results in a higher lattice relative density than the nominal. Component height is also critical because of sintering-related errors, as well as external porosity within the cylindrical lattice shell, which can limit heat transfer from the inside of the tube to the outside. Component height is a driving variable also for the application due to the requirement of stacking multiple supports inside the reactor tubes. The tube loading procedure that was employed in this work enabled to reduce of the heat transfer limitations given by contact resistances without machining the lattice sample. Heat transfer tests performed in several operative conditions showed the excellent heat transfer performances of the produced samples over standard and state-of-the-art catalytic supports, paving the way for the application of samples manufactured with the proposed technique for intensified catalytic reactors.

8. Future work

Regarding the catalytic supports printed with the metal AM extrusion, a future step will be deepening the functional analysis of these structures by including the loading of the lattice structure with porous refractory spherical elements (resulting in mechanical loading of the struts) and pilot plant testing with methane at 800°C and subsequent thermomechanical fatigue testing of the components.

For investigating the industrial applicability of the proposed solution in wider terms, a comparison of the manufacturability, the production costs and the functional capability of the printed catalytic lattice supports made of pure copper with other more productive metal AM techniques (e.g., high-power, or green light L-PBF and Binder Jetting) will be required.

At the same time, studying the scale-up opportunities of this 3D printed solution, including brazing/welding of multiple components, is also a primary importance.

From the functionality point of view, additional heat transfer tests will be necessary to completely identify the heat transfer mechanism inside the 3D printed structure that will include the detailed modelling of the gas and solid phases and allow for the 2D detailed model for catalytic systems employing copper lattices.

9. Acknowledgements

The present research was partially funded by ACCORDO Quadro ASI-POLIMI "Attività di Ricerca e Innovazione" n. 2018-5-HH.0, collaboration agreement between the Italian Space Agency and Politecnico di Milano.

10. References

[1] Zhang XZ, Tang HP, Wang J, Jia L, Fan YX, Leary M, et al. Additive manufacturing of intricate lattice materials: Ensuring robust strut additive continuity to realize the design potential. Addit Manuf 2022;58:103022. https://doi.org/10.1016/j.addma.2022.103022.

[2] Rashed MG, Ashraf M, Mines RAW, Hazell PJ. Metallic microlattice materials: A current state of the art on manufacturing, mechanical properties and applications. Mater Des 2016;95:518–33. https://doi.org/10.1016/j.matdes.2016.01.146.

[3] Meyer G, Musekamp J, Göbel F, Gardian F, Mittelstedt C.

Manufacturability investigation of inclined AlSi10Mg lattice struts using selective laser melting. Manuf Lett 2022;31:101–5. https://doi.org/10.1016/j.mfglet.2021.08.002.

[4] Dallago M, Zanini F, Carmignato S, Pasini D, Benedetti M. Effect of the geometrical defectiveness on the mechanical properties of SLM biomedical Ti6Al4V lattices. Procedia Struct Integr 2018;13:161–7. https://doi.org/10.1016/j.prostr.2018.12.027.

[5] Choong YH, Krishnan M, Gupta M. Recent Advances in the 3D Printing of Pure Copper Functional Structures for Thermal Management Devices. Technologies 2023;11:141. https://doi.org/10.3390/technologies11050141.

[6] Jadhav SD, Goossens LR, Kinds Y, Hooreweder B Van, Vanmeensel K. Laser-based powder bed fusion additive manufacturing of pure copper. Addit Manuf 2021;42:101990. https://doi.org/10.1016/j.addma.2021.101990.

[7] Jiang Q, Zhang P, Yu Z, Shi H, Wu D, Yan H, et al. A review on additive manufacturing of pure copper. Coatings 2021;11. https://doi.org/10.3390/coatings11060740.

[8] Parenti P, Puccio D, Semeraro Q, Colosimo BM. A techno-economic approach for decision-making in metal additive manufacturing: metal extrusion versus single and multiple laser powder bed fusion. Prog Addit Manuf 2023. https://doi.org/10.1007/s40964-023-00442-7.

[9] Singh G, Missiaen JM, Bouvard D, Chaix JM. Copper extrusion 3D printing using metal injection moulding feedstock: Analysis of process parameters for green density and surface roughness optimization. Addit Manuf 2021;38:101778. https://doi.org/10.1016/j.addma.2020.101778.

[10] Jiang D, Ning F. Material extrusion of stainless-steel plate-lattice structure : Part shrinkage , microstructure , and mechanical performance. Manuf Lett 2022;33:712–8. https://doi.org/10.1016/j.mfglet.2022.07.087.

[11] Shaikh MQ, Graziosi S, Atre SV. Supportless printing of lattice structures by metal fused filament fabrication (MF3) of Ti-6Al-4V: design and analysis. Rapid Prototyp J 2021;27:1408–22. https://doi.org/10.1108/RPJ-01-2021-0015.

[12] Malas A, Saleh E, Giménez-López M del C, Rance GA, Helps T, Taghavi M, et al. Reactive Jetting of High Viscosity Nanocomposites for Dielectric Elastomer Actuation. Adv Mater Technol 2022;7:1–11. https://doi.org/10.1002/admt.202101111.

[13] Marleen Rombouts, Jo Verwimp SM. Additive Manufacturing of Metals by 3D Micro-Extrusion of Powder Filled Paste. Eur Powder Metall Assoc Proc Eur Conf 2021. https://doi.org/Additive Manufacturing of Metals by 3D Micro-Extrusion of Powder Filled Paste.

[14] Parenti P, Puccio D, Colosimo BM, Semeraro Q. A new solution for assessing the printability of 17-4 PH gyroids produced via extrusion-based metal AM. J Manuf Process 2022;74:557–72. https://doi.org/10.1016/j.jmapro.2021.12.043.

[15] Horn TJ, Gamzina D. Additive Manufacturing of Copper and Copper Alloys. Addit. Manuf. Process., ASM International; 2020, p. 388–418. https://doi.org/10.31399/asm.hb.v24.a0006579.

[16] Ambrosetti M, Balzarotti R, Fratalocchi L, Bracconi M, Groppi G, Tronconi E. Structured Catalysts and Non-conventional Reactor Designs for Energy Applications. Heterog. Catal. Energy Appl., The Royal Society of Chemistry; 2020, p. 361–96. https://doi.org/10.1039/9781788019576-00361.

[17] Ferri G, Ambrosetti M, Beretta A, Groppi G, Tronconi E. Experimental investigation and 2D mathematical modelling of copper foams packed with Rh-Al2O3 catalysts for the intensification of methane steam reforming. Catal Today 2024;426:114386. https://doi.org/10.1016/j.cattod.2023.114386.

[18] Danaci S, Protasova L, Snijkers F, Bouwen W, Bengaouer A, Marty P. Innovative 3D-manufacture of structured copper supports post-coated with catalytic material for CO 2 methanation. Chem Eng Process - Process Intensif 2018;127:168–77. https://doi.org/10.1016/j.cep.2018.03.023.

[19] Minette F, de Almeida LC, Ratan S, De Wilde J. Pressure drop and heat transfer of ZoneFlow <math altimg="si8.svg" display="inline" id="d1e2379"> <msup> <mrow/> <mrow> <mtext>TM</mtext> </mrow> </msup> </math> structured catalytic reactors and reference pellets for Steam Methane Reforming. Chem Eng J 2021;417:128080. https://doi.org/10.1016/j.cej.2020.128080.

[20] Tronconi E, Groppi G, Visconti CG. Structured catalysts for non-adiabatic applications. Curr Opin Chem Eng 2014;5:55–67. https://doi.org/10.1016/j.coche.2014.04.003.

[21] Fratalocchi L, Groppi G, Visconti CG, Lietti L, Tronconi E. Packed-POCS with skin: A novel concept for the intensification of non-adiabatic catalytic processes demonstrated in the case of the Fischer-Tropsch synthesis. Catal Today 2022;383:15–20. https://doi.org/10.1016/j.cattod.2020.12.031.

[22] Balzarotti R, Bisaccia A, Tripi MC, Ambrosetti M, Groppi G, Tronconi E. Production and characterization of copper periodic open cellular structures made by <scp>3D</scp> printing-replica technique. J Adv Manuf Process 2020;2. https://doi.org/10.1002/amp2.10068.

[23] Desktop Metal. Studio System (TM), https://www.desktopmetal.com/products/studio. (Accessed March 31, 2022) n.d.

[24] Colosimo BM, Grasso M, Garghetti F, Rossi B. Complex geometries in additive manufacturing: A new solution for lattice structure modeling and monitoring. J Qual Technol 2022;54:392–414. https://doi.org/10.1080/00224065.2021.1926377.

[25] Oosterbeek RN, Jeffers JRT. StrutSurf: A tool for analysis of strut morphology and surface roughness in additively manufactured lattices. SoftwareX 2022;18:101043. https://doi.org/10.1016/j.softx.2022.101043.

[26] Ambrosetti M, Groppi G, Schwieger W, Tronconi E, Freund H. Packed Periodic Open Cellular Structures – an Option for the Intensification of Non-Adiabatic Catalytic Processes. Chem Eng Process - Process Intensif 2020;155:108057. https://doi.org/10.1016/j.cep.2020.108057.